

An improved MHD simulation of the 2006 December 13 coronal mass ejection of active region NOAA 10930

YUHONG FAN¹

¹*High Altitude Observatory, National Center for Atmospheric Research,
3080 Center Green Drive, Boulder, CO 80301, USA*

ABSTRACT

We present a magnetohydrodynamic (MHD) simulation of the coronal mass ejection (CME) on 13 December 2006 in the emerging δ -sunspot active region 10930, improving upon a previous simulation by Fan (2016) as follows. (1) Incorporate an ambient solar wind instead of using a static potential magnetic field extrapolation as the initial state. (2) In addition to imposing the emergence of a twisted flux rope, also impose at the lower boundary a random electric field that represents the effect of turbulent convection, which drives field-line braiding and produces resistive and viscous heating in the corona. With the inclusion of this heating, which depends on the magnetic field topology, we are able to model the synthetic soft X-ray images that would be observed by the X-Ray Telescope (XRT) of the Hinode satellite, produced by the simulated coronal magnetic field. We find that the simulated pre-eruption magnetic field with the build up of a twisted magnetic flux rope, produces synthetic soft X-ray emission that shows qualitatively similar morphology as that observed by the Hinode/XRT for both the ambient coronal loops of the active region and the central inverse-S shaped “sigmoid” that sharpens just before the onset of the eruption. The synthetic post-flare loop brightening also shows similar morphology as that seen in the Hinode/XRT image during the impulsive phase of the eruption. It is found that the kinematics of the erupting flux rope is significantly affected by the open magnetic fields and fast solar wind streams adjacent to the active region.

Keywords: magnetohydrodynamics(MHD) — methods: numerical — Sun: corona — Sun: coronal mass ejections (CMEs) — Sun: filaments, prominences

1. INTRODUCTION

Significant progress has been made in theory and numerical simulations to understand the basic magnetic configurations and mechanisms for the onset of major solar eruptions such as eruptive flares and coronal mass ejections (e.g. reviews by Forbes et al. 2006; Chen 2011; Green et al. 2018). Recently, MHD simulations that use observed data to construct the initial state and the boundary driving conditions are being developed and are playing an increasingly important role in studying the realistic complex magnetic field evolution in observed solar eruptive events (e.g. Jiang et al. 2013; Kliem et al. 2013; Inoue et al. 2014; Amari et al. 2014; Fan 2016; Hayashi et al. 2018; Török et al. 2018; Guo et al. 2019; Liu et al. 2022).

Fan (2011, 2016) and Amari et al. (2014) have carried out MHD simulations to model the magnetic field evolution of the X3.4 flare and the associated halo CME that occurred on December 13, 2006 in active region (AR) 10930. The photospheric magnetic field evolution of AR 10930 was characterized by an emerging positive polarity spot against the southern edge of a dominant pre-existing negative spot. The emerging positive spot showed substantial counter-clockwise rotation (by 540°) and eastward motion as it grew (Min & Chae 2009), suggesting the emergence of a twisted magnetic flux rope. Motivated by this observation, Fan (2016) modeled the pre-eruption magnetic field by imposing at the lower boundary the (partial) emergence of an east-west oriented magnetic torus into an initial potential coronal magnetic field extrapolated from a smoothed magnetogram from the Solar and Heliospheric Observatory (SOHO)/Michelson Doppler Imager (MDI) about 6 hours before the flare. An east-west oriented magnetic flux rope

with more than 1 wind of total twist is built up quasi-statically in the corona and subsequently erupts to produce a CME in the MHD simulation. The simulated magnetic field evolution is able to qualitatively explain several observed features of the event seen in the images by the X-Ray Telescope (XRT) on board the Hinode satellite, including the formation of an X-ray sigmoid brightening just before the onset of the eruption and the morphology of the post-flare loop brightening during the impulsive phase of the flare. Amari et al. (2014) modeled the pre-eruption magnetic field evolution by constructing a sequence of force-free field solutions extrapolated from the observed photosphere vector magnetograms from the Solar Optical Telescope (SOT) of Hinode. They also found the formation of a twisted magnetic flux rope with more than 1 wind of twist in the pre-eruption magnetic field just before the onset of the observed major eruption. They further carried out an MHD simulation of the subsequent dynamic evolution using the force-free field solution as the initial state, driven with the appropriated lower boundary conditions, and found the loss of equilibrium of the flux rope that produced a CME.

For all the above models, the comparisons with observations have been limited to identifying the morphology of selected field lines with certain features in the observables such as the soft X-ray emission observed by the Hinode/XRT. Also for the above simulations, the initial ambient corona is modeled with a static, potential magnetic field configuration, without considering the effect of the solar wind outflows. In this work, we improve upon the simulation of Fan (2016) by incorporating a more explicit treatment of the background coronal heating that represents the effect of turbulent convection and varies self-consistently based on the formation of the strong current layers in the 3D coronal magnetic field. With this heating, we are able to model the synthetic soft X-ray emission as would be observed by the Hinode/XRT produced by the simulated coronal magnetic field of the active region. This allows a more direct comparison with the observation. With this background coronal heating, we also initialize a partially open coronal magnetic field with a background solar wind as the initial state for our simulation of the event. In section 2 we describe the MHD model and the setup of the improved simulation. The result of the simulation is shown in section 3 and a summary and discussion is given in section 4

2. MODEL DESCRIPTION

In this simulation, we use the “Magnetic Flux Eruption” (MFE) code to solve the set of semi-relativistic MHD equations as described in Fan (2017). Compared to the previous simulation of Fan (2016), a more sophisticated treatment of the thermodynamics is used where the internal energy equation explicitly takes into account the non-adiabatic effects in the corona, including the field-aligned thermal conduction, optically thin radiative cooling, and coronal heating. The readers are referred to Fan (2017) for the MHD equations being solved and a description of the numerical methods. Here we only describe the modifications made in the current numerical model relative to Fan (2017). For the heating term in the internal energy equation (term H in eq. (5) of Fan 2017), we no longer include the empirical coronal heating (eq. (14) in Fan 2017), but only include the heating resulting from the dissipation of the kinetic and magnetic energies due to the numerical diffusion effects (see the description in the first paragraph on p.3 of Fan 2017). As described later in this section, for this simulation, we impose at the lower boundary a random electric field representing the effect of turbulent convection that drives field line braiding, and the resultant (numerical) resistive and viscous dissipation of the magnetic and kinetic energies provides the necessary heating of the corona. The heating varies spatially and temporally self-consistently with the locations of the strong current layers that form in the 3D magnetic field.

We set up the initial state with a background solar wind as follows. The white boxed region on the MDI full-disk magnetogram at 20:51:01 UT on December 12 (Figure 1(a)) is extracted as the lower boundary of the spherical wedge simulation domain, for which the emerging active region is centered at $\theta = 0$ and $\phi = 0$ in the simulation spherical coordinates as shown in Figure 1(b). The radial extent of the simulation domain is from $1R_{\odot}$ to $10R_{\odot}$, where R_{\odot} is the solar radius. The latitudinal and longitudinal widths of the simulation domain are respectively 117.2° and 98.3° , centered on the active region. The spherical wedge simulation domain is resolved with a grid of $832(r) \times 480(\theta) \times 504(\phi)$ that is stretched in all three directions such that the highest grid resolution (1.03 Mm) is near the lower boundary and centered on the active region. A potential field extrapolation from the photosphere normal magnetic field at the domain’s lower boundary shown in Figure 1(b) is carried out. Then the radial magnetic field in the horizontal plane at 14 Mm height of the extrapolated potential field, with a central area corresponding to the region of the observed flux emergence zeroed out, is used as the initial lower boundary normal magnetic field (Figure 1(c)) for the simulation. It is considered as the pre-emergence normal magnetic field at the base of the corona. We then initialize the domain with a potential field extrapolated from this lower boundary normal magnetic field (shown in Figure 1(c)) together with a

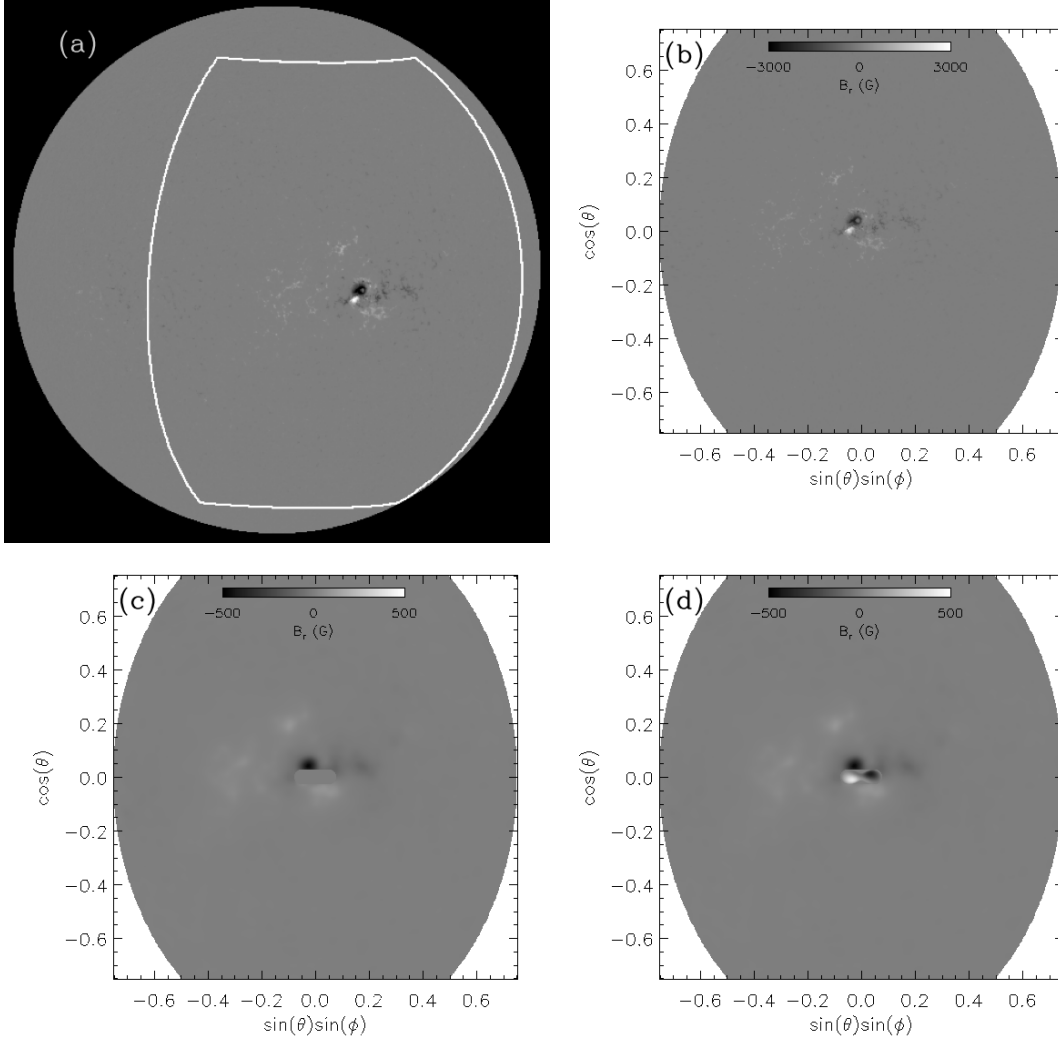


Figure 1. (a) SOHO MDI full-disk magnetogram at 20:51:01 UT on 2006 December 12. The white box encloses the area to be used as the lower boundary of the simulation domain. (b) Radial magnetic field B_r in the region enclosed by the white box in (a) as viewed straight on at the center of the emerging active region. (c) B_r of the extrapolated potential field (extrapolated from the B_r in (b)) in the horizontal slice at 14 Mm height and with the field in a central region zeroed out, where the emergence of a twisted magnetic torus is to be imposed. This B_r is the initial lower boundary normal magnetic field for the simulation. (d) B_r on the lower boundary at the time of the impulsive phase of the eruption in the simulation.

hydrostatic atmosphere, and numerically evolve the coronal domain driven at the lower boundary with the following random, horizontal electric field $\mathbf{E}_h^{\text{random}}$:

$$c\mathbf{E}_h^{\text{random}} = -\nabla_h(\xi B_r). \quad (1)$$

In the above c denotes the speed of light, the subscript h denotes the horizontal directions perpendicular to the r (radial) direction, B_r is the normal magnetic field in the lower boundary and ξ is a time dependent field that is made up of a superposition of 62402 randomly placed cells of opposite sign values. Each of the cells is spatially a 2D Gaussian profile with a size scale of 5.22 Mm and a central amplitude of $8.14 \times 10^{14} \text{ cm}^2/\text{s}$, and temporally a sinusoidal function with a period and life time of 11.89 min. A snapshot of the ξ field is illustrated in Figure 2 with a movie showing the evolution of the time-dependent ξ field in the online version of the paper. $\mathbf{E}_h^{\text{random}}$ effectively drives random rotations of the footpoints of the B_r flux concentrations, with positive (negative) ξ corresponding to clockwise (counter-clockwise) rotation. Note, since $\mathbf{E}_h^{\text{random}}$ is given as the gradient of a potential (eq. [1]), it does not produce any change of B_r on the surface and therefore preserves the (observed) normal magnetic flux distribution. Here with

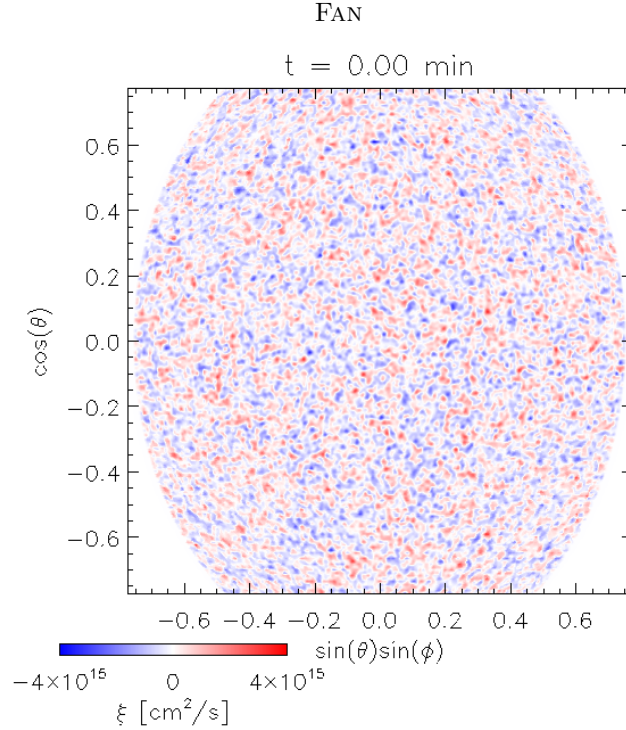


Figure 2. A snapshot of the ξ field used in specifying $\mathbf{E}_h^{\text{random}}$ in equation (1). An animated version of the figure is available, which shows the evolution of the random cellular pattern of the ξ field for about 5 hours.

the use of the staggered grid and the constrained transport scheme (e.g. Stone & Norman 1992), the zero-circulation nature of $\mathbf{E}_h^{\text{random}}$ and hence the zero change of B_r is enforced numerically to machine precision at the lower boundary surface. $\mathbf{E}_h^{\text{random}}$ represents the effect of turbulent convection that drives field line braiding and produces (numerical) resistive and viscous heating in the corona. Many past numerical studies have used similar ways of driving coronal heating by imposing random motions representative of the turbulent convection at the photospheric lower boundary of the MHD simulations (e.g. Gudiksen & Nordlund 2005; Warnecke & Peter 2019).

We note that the $\nabla_h(\xi B_r)$ used for the random electric field in equation (1) is of the same form as the $\nabla_s(\zeta B_n)$ used for the lower boundary electric field in the STITCH (STatistical InjecTion of Condensed Helicity) subgrid model described in Dahlin et al. (2021, see eq. (1) in that paper), with ∇_h corresponding to ∇_s , ξ to ζ , and B_r to B_n . The difference is that a large-scale, like-signed ζ field is used in the STITCH electric field. In contrast, the random electric field here uses a collection of small-scale cells of random signs for the ξ field. Thus here the random electric field represents the driving effect of a small-scale turbulent convection with no net helicity transported into the corona. On the other hand the STITCH electric field represents a large-scale statistical mean effect of a helical convection that builds up net helicity in the corona (Mackay et al. 2014; Dahlin et al. 2021).

The treatment of the thermodynamic conditions at the lower boundary is the same as that described in (Fan 2017, see eqs. (17)(18) and the associated text in that paper). The boundary conditions for the side and the top boundaries are also the same as Fan (2017).

We numerically evolve the corona domain driven with the above random electric field at the lower boundary until it reaches a quasi-steady partially open coronal magnetic field with a background solar wind as shown in Figure 3. This is then used as the initial state for the subsequent simulation of the build up and eruption of the CME magnetic field driven by flux emergence at the lower boundary. For the initial state, we see low-latitude open coronal-hole magnetic fields adjacent to the closed fields of the active region on both its east and west sides. There are strong solar wind outflows emanating from the dominant pre-existing negative sunspot and the adjacent region to the west of the spot, as can be seen from the (red) radial velocity v_r in the r - ϕ slice extending from the active region. The open magnetic field lines show large wiggles and kinks, which correspond to the large amplitude Alfvén waves driven by the random electric field at the lower boundary.

The random electric field imposed at the lower boundary drives a Poynting flux through the coronal domain, whose time and horizontally averaged radial profile of the flux density $S_r = \langle (c/4\pi)(\mathbf{E} \times \mathbf{B})_r \rangle$ is shown in Figure 4, where

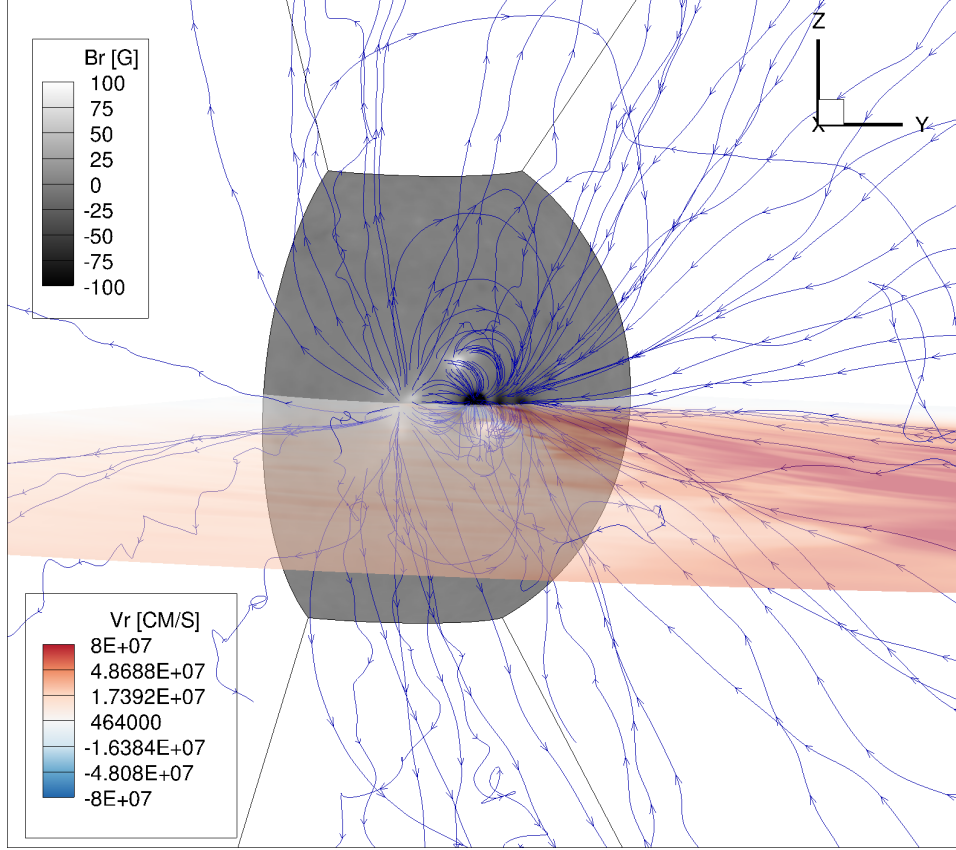


Figure 3. The quasi-steady initial state containing a partially open coronal magnetic field with a background solar wind. Blue lines are magnetic field lines with arrows marking the magnetic field directions. A r - ϕ slice at the latitude of the dominant pre-existing negative sunspot of the active region is shown with color indicating the radial velocity. The gray-scale colored bottom boundary surface shows the normal magnetic field B_r . The open magnetic field lines show large wiggles and kinks, which are due to the large amplitude Alfvén waves driven by the random electric field at the lower boundary.

$\langle \rangle$ represents averaging over spherical shells and over time (for about 10 hours in the quasi-steady state). The divergence of the Poynting flux provides the energy input for heating the corona and accelerating the solar wind (e.g. Rempel 2017). The averaged upward Poynting flux density at the lower boundary (base of the corona) is found to be $5.3 \times 10^5 \text{ erg/s/cm}^2$, which is consistent with the necessary energy flux to sustain the heating of the quiet-sun corona (e.g. Withbroe 1988; Rempel 2017). The r.m.s. velocity near the lower boundary is found to be about 13 km/s, compared to the mean sound speed of 117 km/s and the mean Alfvén speed of 615 km/s. Thus the velocities near the lower boundary resulting from the random electric field are very sub-sonic and sub-alfvénic. Figure 5 shows the radial profiles of the horizontally averaged temperature, density, Alfvén speed, sound speed, and radial flow speed of the quasi-steady initial state. It can be seen that reasonable mean temperature, density profiles of the corona are maintained. The (horizontally averaged) mean Alfvén speed significantly exceeds the mean sound speed for most of the height range of the domain. The mean radial outflow speed exceeds the mean sound speed at about 4 solar radii and exceeds the mean Alfvén speed at about 7 solar radii.

With the above numerically evolved quasi-steady state as the initial state, we then impose at the lower boundary, in addition to the above random electric field, the emergence of an east-west oriented twisted magnetic torus in the zeroed-out region with the electric field $\mathbf{E}_h^{\text{emg}}$:

$$c\mathbf{E}_h^{\text{emg}} = -(\mathbf{v}_{\text{rise}} \times \mathbf{B}_{\text{tube}})_h, \quad (2)$$

that corresponds to the rise of a magnetic torus \mathbf{B}_{tube} at a constant velocity \mathbf{v}_{rise} through the lower boundary, as was done in Fan (2016). The expressions for \mathbf{B}_{tube} and \mathbf{v}_{rise} are given in Fan (2016, see eqs. (4)-(7) and the associated text in that paper) with the following changed values of the parameters for the torus: the minor radius of the torus is $a = 0.028R_\odot$ and the major radius is $R' = 0.0504R_\odot$, the rate of field-line twist about the curved axis of the torus is

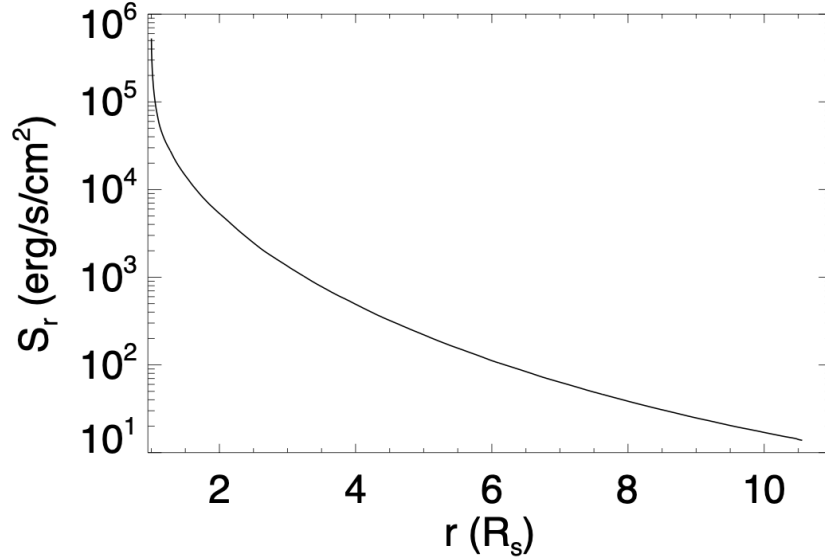


Figure 4. Radial profile of the time and horizontally averaged Poynting flux density (see text for the expression of S_r) for the quasi-steady initial state.

$q/a = 0.102 \text{ rad/Mm}$, the field strength at the curved axis of the torus is $B_t a/R' = 361 \text{ G}$, the center of the torus is initially located at $(r_c = 0.922 R_\odot, \theta_c = 90^\circ, \phi_c = 0^\circ)$ in the simulation spherical coordinate system and is assumed to be rising at a constant velocity $\mathbf{v}_{\text{rise}} = v_{\text{rise}} \hat{\mathbf{r}}_c$ with $v_{\text{rise}} = 3.9 \text{ km/s}$. In this simulation, the pre-emergence lower boundary (base of the corona) magnetic field (see Figure 1(c)) is obtained from the extrapolated potential field at 14 Mm height, and has a significantly stronger peak strength (peaks at about 500 G) than that used for the lower boundary (peaks at about 200 G) in the simulation of Fan (2016), which is obtained by heavily smoothing the photosphere magnetogram. Because of this, in this simulation we also use a significantly stronger, more compact magnetic torus for the imposed flux emergence, as given by the above changed parameters, compared to that used in the Fan (2016). At the end of the imposed flux emergence in the simulation, the total emerged (unsigned) flux is approximately equal to the total flux originally in the zeroed out area in Figure 1(c). In summary, in this simulation, we impose at the lower boundary $\mathbf{E}_h^{\text{emg}} + \mathbf{E}_h^{\text{random}}$, where $\mathbf{E}_h^{\text{emg}}$ drives the emergence of a twisted magnetic torus to build up the twisted pre-eruption coronal magnetic field, while the random electric field $\mathbf{E}_h^{\text{random}}$ continues to drive the background corona heating.

3. SIMULATION RESULTS

Figure 6 shows a sequence of snapshots of the evolution of the 3D magnetic field lines (left column a zoomed-in view, middle column a far view) and the synthetic Hinode/XRT images (right column) produced by the simulation. The synthetic XRT images are computed by integrating along the line of sight (LOS) as viewed from earth, through the simulation domain:

$$I_{\text{XRT}} = \int n_e^2(l) f_{\text{Be.thin}}(T(l)) dl, \quad (3)$$

where l denotes the length along the LOS through the simulation domain, I_{XRT} denotes the modeled intensity in XRT Be.thin channel (shown in the right column images in Figure 6 in LOG scale), n_e is the electron number density, and $f_{\text{Be.thin}}(T(l))$ is the instrument temperature response function for the Be.thin channel obtained by calling `make_xrt_wave_resp` and `make_xrt_temp_resp` functions in the IDL SolarSoft XRT package.

Due to the imposed flux emergence by $\mathbf{E}_h^{\text{emg}}$ at the lower boundary, a twisted magnetic flux rope is built up quasi-statically in the corona over the time period from $t = 0$ to about $t = 2.4 \text{ hr}$, and an inverse-S shaped sigmoid brightening develops in the synthetic XRT images (see the two top rows in Figure 6 and the associated movie). During this time period the total magnetic energy (E_m) and the free magnetic energy ($E_m - E_p$, where E_p is the corresponding potential field magnetic energy) show an overall increase as can be seen in Figures 7(a)(b) (for $t = 0$ to roughly $t = 2.4 \text{ hr}$), while the emerging flux rope remains confined by the closed field of the active region with the kinetic energy maintaining

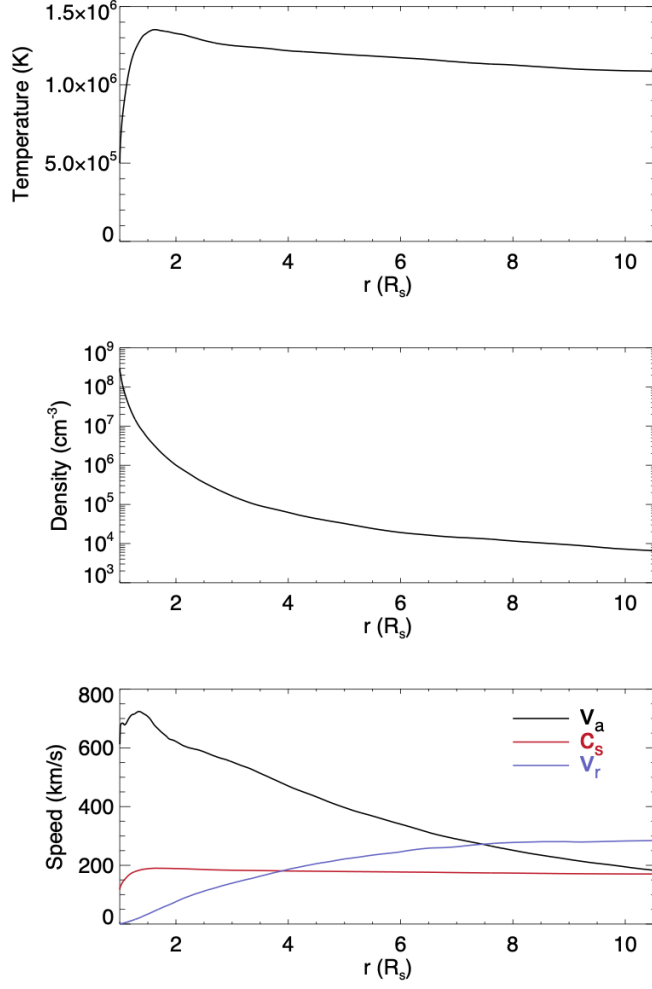


Figure 5. Radial profiles of the horizontally averaged temperature (top), density (middle), and Alfvén speed, sound speed, and radial flow speed (bottom) of the quasi-steady initial state.

roughly steady at the level of the ambient solar wind (Figure 7(c)). In Figure 7(d), we show the various contributions to the rate of change of the total magnetic energy (dE_m/dt) due to: the input of magnetic energy by the Poynting flux integrated over the boundaries (black curve), the release of magnetic energy resulting from the Lorentz force work (solid red curve), the release of magnetic energy by the numerical resistive dissipation (red dashed-dotted curve), and the sum of the above source and sinks (blue curve). During the quasi-static phase (from $t = 0$ to about $t = 2.4$ hr), we see that the energy input by the Poynting flux integrated over the boundaries is for most of the time greater than the sum of the total magnetic energy release in the domain by the Lorentz force work and the numerical resistive dissipation, and thus the magnetic energy builds up over this period. The magnetic energy release due to the Lorentz force work is generally smaller than that due to the numerical resistive dissipation in this simulation. We see that the numerical resistive dissipation increases gradually during the quasi-static phase due to the flux emergence. On the other hand the magnetic energy release due to the Lorentz force work remains relatively small because the emerged flux rope remains confined in a quasi-static state.

At about $t = 2.5$ hr there is a sharp increase of the magnetic energy release by the Lorentz force work (red solid curve in Figure 7(d)), which coincides with a rapid acceleration of the flux rope (see Figure 7(e)) and a rapid increase of the total kinetic energy (Figure 7(c)), indicating the loss of equilibrium and eruption of the flux rope. Both the Lorentz force work and the numerical resistive dissipation show a sharp increase (red curves in Figure 7(d)), resulting in a relatively sharp decrease in the magnetic energy (Figures 7(a)(b), at about $t = 2.5$ hr). After this sudden release of the magnetic energy, the magnetic energy gradually turns to increasing with time again (Figures 7(a)(b)) due to

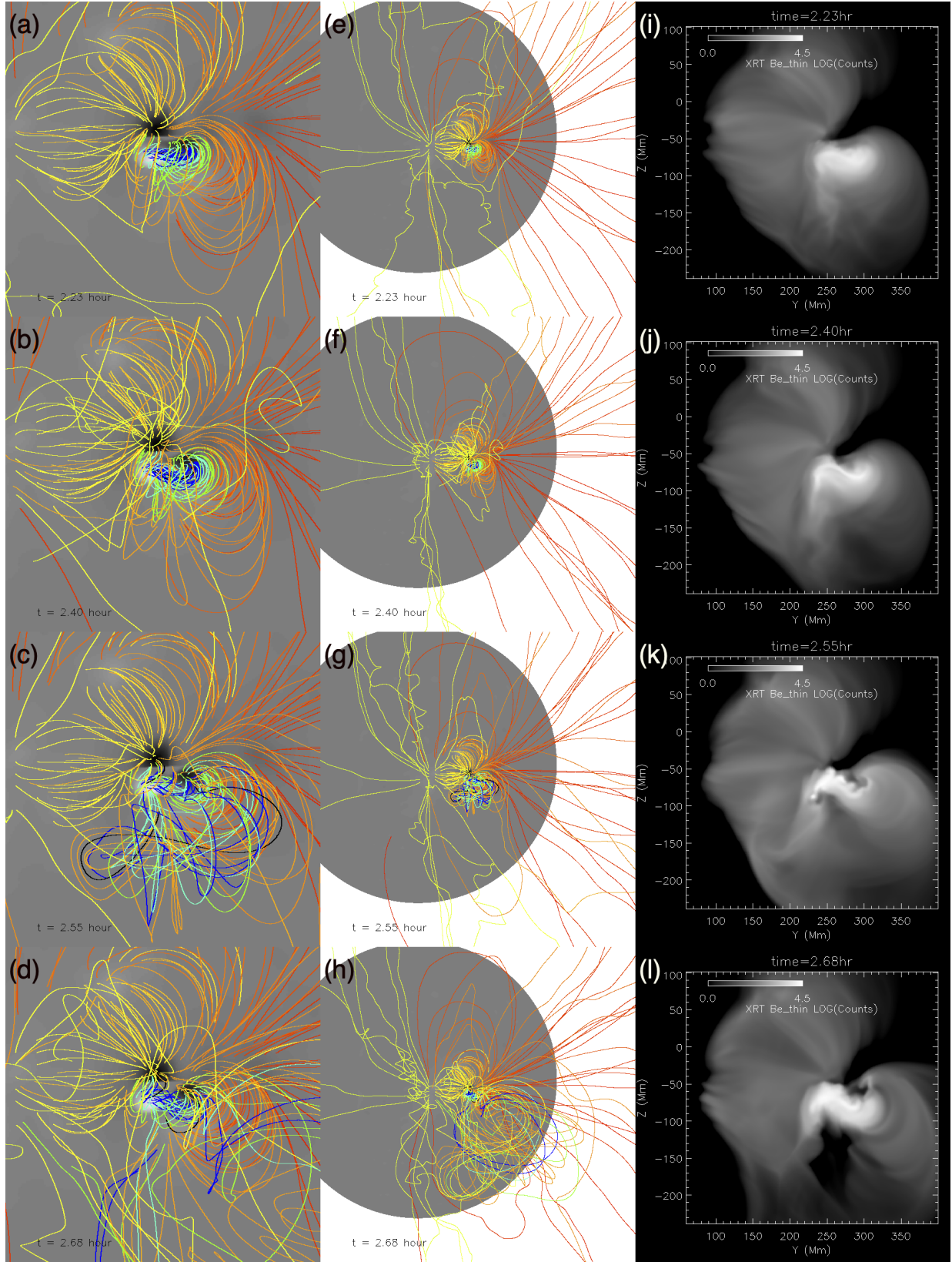


Figure 6. Snapshots showing the evolution of the 3D magnetic field lines (left column: a zoomed-in view, middle column: a far view) and the synthetic Hinode/XRT images (right column). An animated version of this figure is available, which shows the entire 3.96 hours of the simulated evolution from the beginning of the driving flux emergence through the eruption. In the animated synthetic X-ray images, it is easier to identify an outgoing band of diffuse brightening that emanates from the sigmoid at about $t = 2.45$ hour and moves southward until leaving the field of view at about $t = 2.58$ hour, which corresponds to the hot core of the erupting flux rope as discussed in the text.

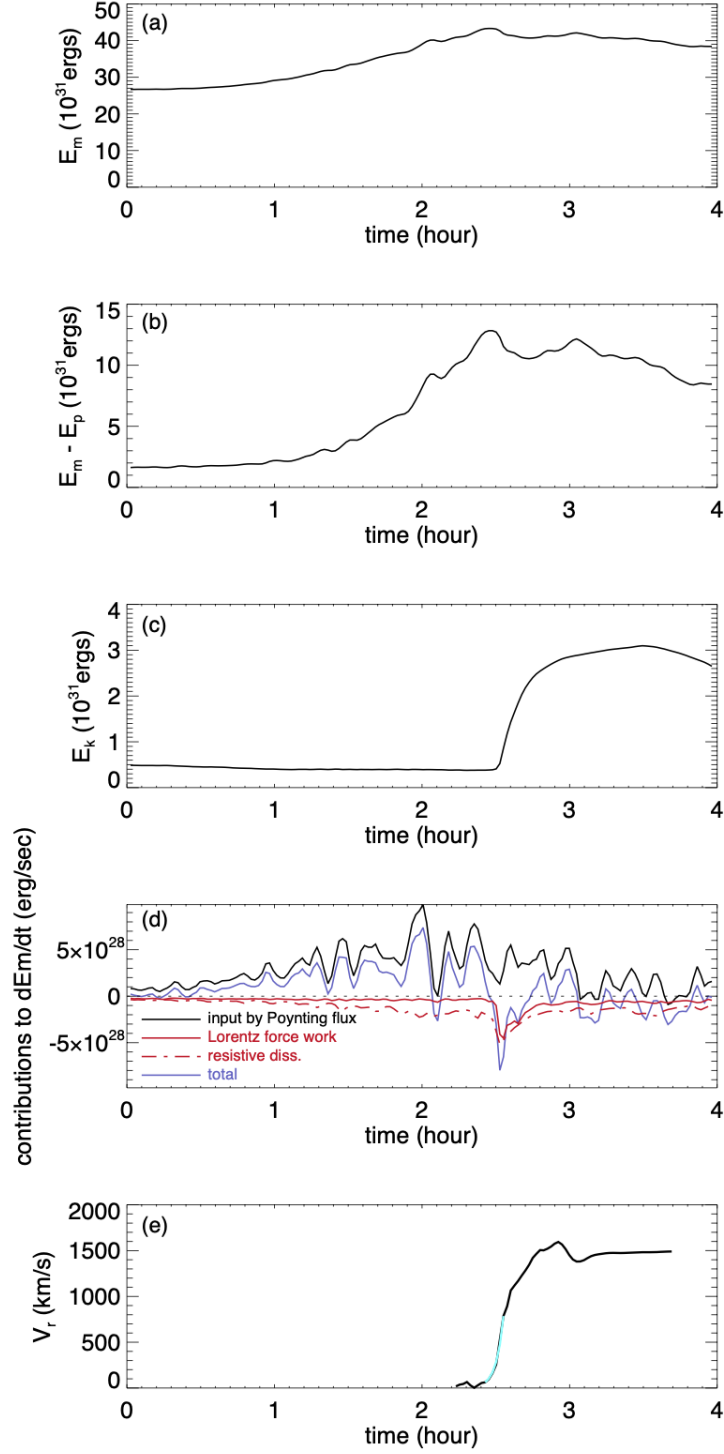


Figure 7. (a) shows the evolution of the total magnetic energy E_m ; (b) shows the evolution of the free magnetic energy $E_m - E_p$, where E_p is the corresponding potential field energy; (c) shows the evolution of the total kinetic energy E_k ; (d) shows the contributions to the rate of change of the total magnetic energy (dE_m/dt) due to: the input of magnetic energy by the Poynting flux integrated over the boundaries (black curve), the release of magnetic energy resulting from the Lorentz force work (solid red curve), the release of magnetic energy by the numerical resistive dissipation (red dashed-dotted curve), and the sum of the above source and sinks (blue curve); (e) shows the evolution of the radial velocity of a Lagrangian tracer point placed in the core field region of the emerged flux rope just before the onset of the eruption (see the green star point in Figure 10) and tracked in the velocity field. The cyan curve is a fitted function of an exponential growth of the radial velocity: $v_r = v_0 \exp((t - t_0)/\tau)$ over the period from time $t_0 = 2.43$ hour to time $t_1 = 2.55$ hour, with $\tau = 176$ sec and $v_0 = 62$ km/s.

the continued magnetic flux emergence imposed at the lower boundary, until about $t = 3$ hr when we stop the imposed flux emergence. The snapshots in Figures 6(c)(g) (at $t = 2.55$ hr) and Figures 6(d)(h) (at $t = 2.68$ hr) show the morphology of some of the erupting twisted field lines. By tracking a Lagrangian tracer placed in the core field region of the emerged flux rope just before the onset of the eruption, we find that its rise speed (Figure 7(e)) undergoes an exponential growth starting from about $t = 2.43$ hr to about $t = 2.55$ hr (see the cyan curve), and it eventually accelerate to a final steady speed of about as 1500 km/s for this tracer point in the erupting flux rope. Thus the time for the onset of eruption of the flux rope is about $t = 2.43$ hour, corresponding to the start of the exponential growth of the rise speed. It reaches a peak acceleration of about 3 km/s^2 at $t = 2.53$ hr. This peak acceleration is in the high end range of the observed peak accelerations of CMEs (e.g. Bein et al. 2011). The high field strength (~ 400 G) of the emerged flux rope at the base of the corona in this simulation certainly contributes to the fast acceleration of the eruption (e.g. Green et al. 2018).

3.1. The pre-eruption magnetic field and the initiation of eruption

We find that the sigmoid brightening in the synthetic XRT images sharpens into a thin sigmoid shape just before (a few minutes before) the onset of the eruption (Figure 6(j)). This is consistent with the observed Hinode/XRT image just before (within a few minutes of) the onset of the X-class flare as shown in a side by side comparison in Figure 8. Overall, the synthetic X-ray emission shows qualitatively similar morphology as the observed Hinode/XRT

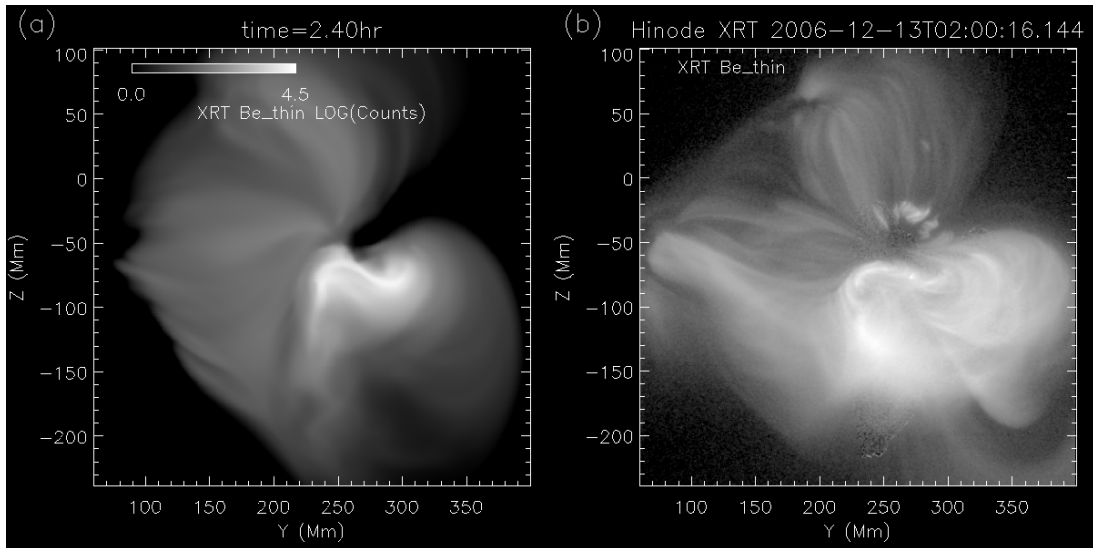


Figure 8. (a) Synthetic Hinode/XRT image at the time a few minutes before the onset of the eruption compared with (b) the observed Hinode/XRT image about 3 minutes before the onset of the X-class flare.

image for both the ambient coronal loops of the active region and the central thin sigmoid brightening. We find that the sharpening of the central sigmoid brightening in the simulation is due to the resistive heating produced by the formation of a sigmoid shaped strong current layer in the lower part of the flux rope as shown in Figure 9. We see that the sigmoid shaped current layer (outlined by the purple iso-surface of current density J) forms in the lower part of the left-hand twisted (blue) fields of the flux rope, and its central portion thins into a vertical sheet aligned with the polarity inversion line (PIL) of the emerging region. One difference we have noticed between the thin sigmoid in the synthetic XRT image and that in the observed one is that the modeled sigmoid appears located more westward by about 10 Mm compared to the observed thin sigmoid. This suggests that an improvement of the model would be to shift the emerging torus driven at the lower boundary eastward by about 10 Mm.

Figure 10 shows, at the start time ($t = 2.43$ hour) of the exponential acceleration of the flux rope, the twist rate $\alpha = \mathbf{J} \cdot \mathbf{B} / B^2$ in the meridional cross-section across the middle of the emerged flux rope, over-plotted with the contours of the decay index, $d(\ln P_h) / d(\ln h)$, of the horizontal component of the corresponding potential field P_h vs height h above the lower boundary surface. It can be seen that a significant portion of the emerged flux rope cross-section (indicated by the dashed arrow) with negative twist rate has entered above the contour of the critical decay index of -1.5 for the onset of the torus instability (e.g. Kliem & Török 2006). This indicates that the onset of the eruption is

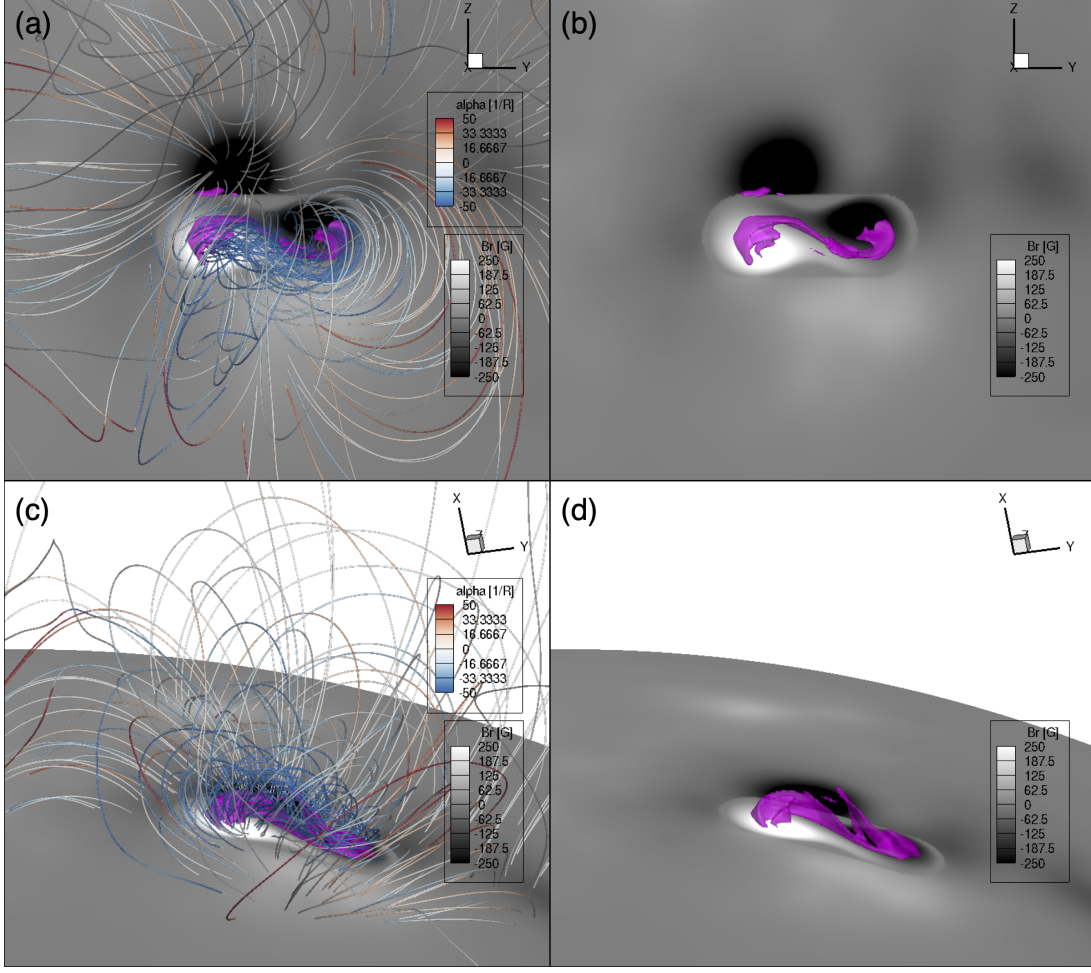


Figure 9. Coronal magnetic field lines colored with the twist rate defined as $\alpha = \mathbf{J} \cdot \mathbf{B}/B^2$ and the (purple) iso-surface of the current density $J = |\nabla \times \mathbf{B}|$ that outlines the thin current layer at the time ($t = 2.4$ hour) just before the onset of the eruption, viewed from the earth perspective (upper panels) and a side view (lower panels).

consistent with the onset of the torus instability of the emerged flux rope. Furthermore, the thinning of the current layer (see the thinning layer of strong α marked by the solid arrow in Figure 10) suggests the development of a current sheet driven by the unstable rise of the flux rope, and that the ensuing rapid reconnections enhance the acceleration of the flux rope. Figure 11 shows the integrated total twist $(1/2\pi) \int (\alpha/2) ds$ of a set of field lines in the emerged flux rope, where the integration is along the arc length s of the field line between the two anchored ends at the lower boundary. The total twist is shown by the color of these field lines. We find that for the central core field lines of the emerged flux rope the total twist has reached about 1.5 winds (or 3π radian of rotation) between the anchored ends, exceeding the critical total twist of 1.25 winds (or 2.5π radian of rotation) for the onset of the kink instability of a line tied twisted flux tube (Hood & Priest 1981). Thus the kink instability may also have contributed to driving the unstable rise in the core field region of the flux rope.

3.2. The erupting magnetic field

During the impulsive phase of the eruption, the central sharp thin sigmoid in the synthetic X-ray image broadens into a bright sigmoid shaped band, as can be seen in Figures 6(k) and 6(l) (see also the associated movie of Figure 6). This central brightening corresponds to the highly heated post-flare (post-reconnection) loops that form due to the rapid reconnection in the current sheet. Figure 12 shows the low-lying field lines of the post-flare loops as viewed from the earth perspective (panels (a),(b),(e),(f)) and a side view of the highly twisted field lines in the erupting flux rope together with the low-lying post-flare loop field lines (panels (d)(h)), at time $t = 2.5$ hour (upper row) and time $t = 2.55$ hour (lower row), which is about the time of the peak acceleration of the flux rope (Figure 7(e)) and also

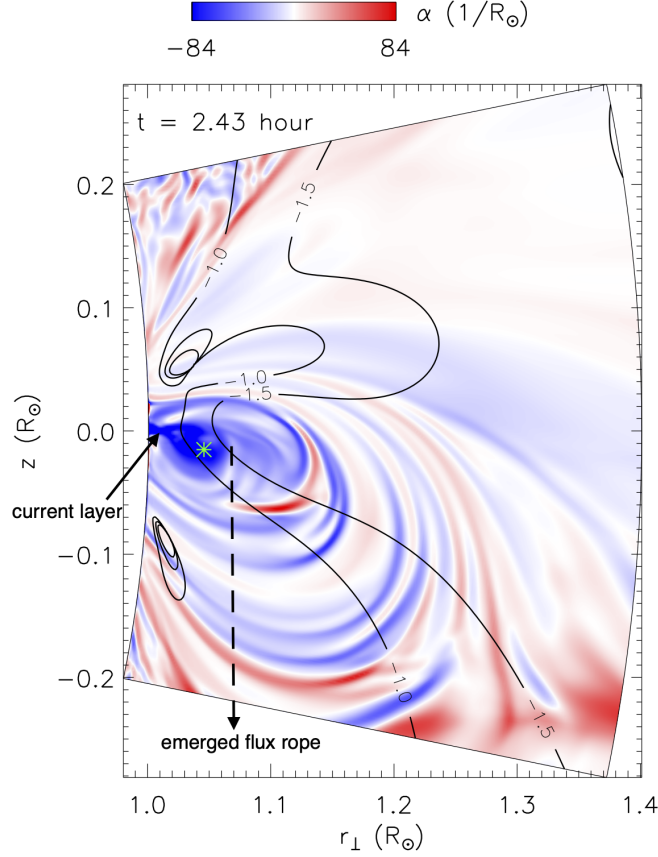


Figure 10. Twist rate α in the meridional cross-section across the middle of the emerged flux rope, over-plotted with the contours of the decay index of the horizontal component of the corresponding potential field (see text for the decay index definition). The dashed arrow marks roughly the center of the emerged flux rope cross-section. The solid arrow points to the thinning current layer near the bottom of the emerged flux rope. The green star point marks the Lagrangian tracer point, whose evolution of the radial velocity is shown in Figure 7(e)

about the time of the peak dissipation of the magnetic energy (Figures 7(d)). In the side view image Figure 12(h), one can see the cusp-shaped tops of the post flare-loops produced by the reconnection in the current sheet extending above the cusp, and the outflow v_r from the current sheet as shown in the central cross-section of the erupting, highly twisted flux rope. The post-flare loops are heated to high temperature with peak temperature exceeding 10^7 K (Figures 12(a)(e)) and are of high density (Figures 12(b)(f)). They have footpoints rooted in the flare ribbons (Figures 12(c)(g)), corresponding to the region of high temperature gradient dT/dr , with strong downward heat conduction flux. The evolution of the post-flare loops and the flare ribbons are consistent with the basic results of the 3D flare reconnection modeled in many previous MHD simulations of erupting flux ropes (e.g. Aulanier et al. 2012; Dahlin et al. 2022). These results include the formation and separation of two J-shaped flare ribbons from the PIL (Figures 12(c)(g)), and the post-flare loops that form initially with a stronger shear (the field component parallel to the PIL) over the central portion of the PIL (Figures 12(a)(b)), compared to those that form later with a weaker shear (Figures 12(e)(f)). The formation of sheared post-flare loops and the strong-to-weak shear transition in time are characteristic features of the 3D flare reconnection with a significant guide field resulting from the shear component of the magnetic field in the erupting flux rope (e.g. Aulanier et al. 2012; Dahlin et al. 2022).

The high-temperature, high-density post-flare loops (e.g. Figures 12(e)(f)) produce the central enhanced emission of a sigmoid shaped band seen in the synthetic X-ray image (e.g. Figure 13(a)). In comparison, the observed XRT image (Figure 13(b)) at the impulsive phase also shows a qualitatively similar sigmoid shaped band of post-flare loops, although the band appears more extended towards both the east and west ends. Note that in the observed XRT image during the impulsive phase, only the central post-flare loops are visible. This is because during the flare phase

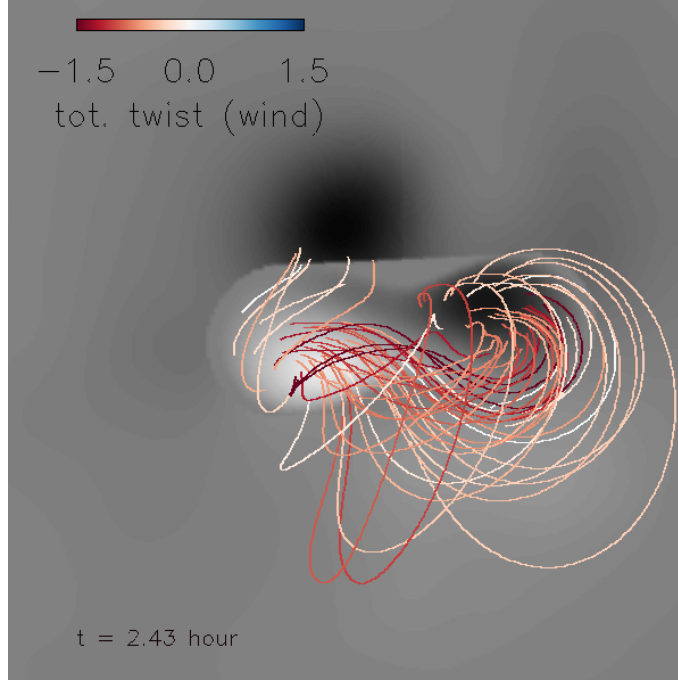


Figure 11. The integrated total twist $(1/2\pi) \int (\alpha/2) ds$ of a set of field lines in the emerged flux rope (at the same time instance as Figure 10), where the integration is along the arc length s of the field line between the two anchored ends at the lower boundary. The total twist is shown by the color of the field lines.

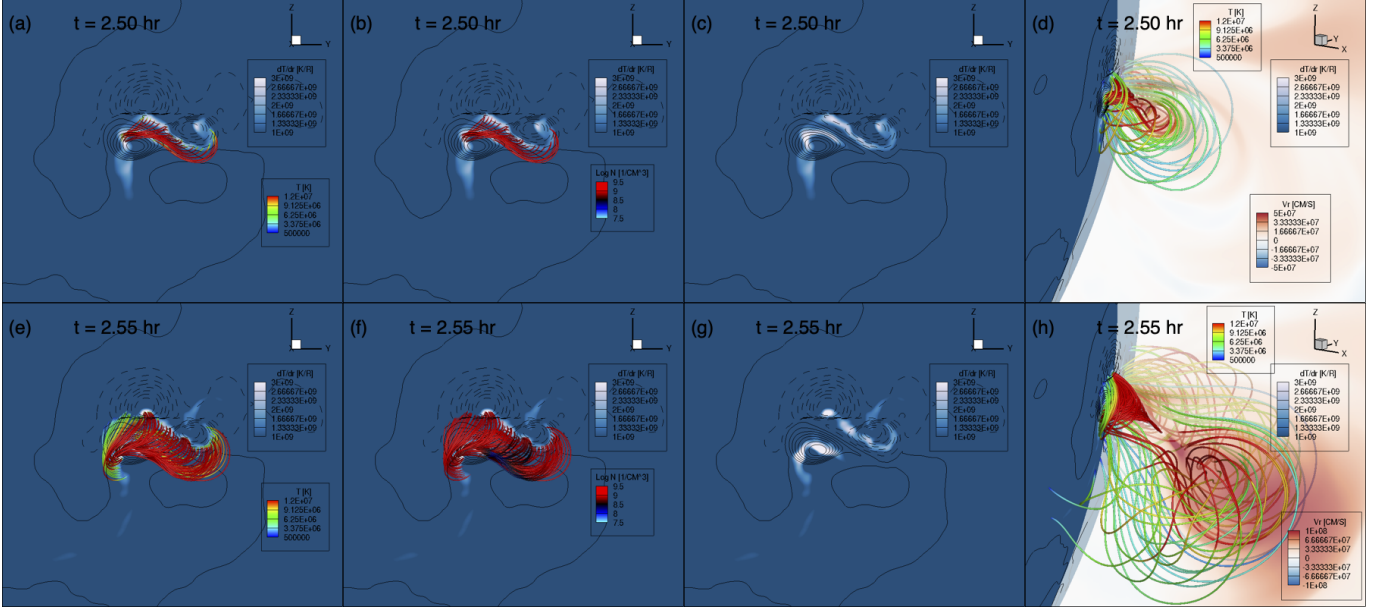


Figure 12. (a)(b)(e)(f) show selected field lines of the the post-flare loops colored with temperature (1st column) and density (2nd column), plotted against the lower boundary image of the temperature gradient dT/dr (with high dT/dr identifying the locations of flare ribbons) and contours of the normal magnetic field B_r , viewed from the earth view point, at two different times (upper row at $t = 2.50$ hour and lower row at $t = 2.55$ hour) during the impulsive phase of the eruption; (c)(g) are the same as (a)(e) but without the post-flare loop field lines; (d)(h) are the same as (a)(e) but a different view from the side, and with the addition of selected field lines of the erupting flux rope and a translucent plane showing the radial velocity v_r in the central meridional cross-section of the erupting flux rope. The lower row images for $t = 2.55$ hour correspond to roughly the time of the peak acceleration of the flux rope and also roughly the time of the peak magnetic energy dissipation.

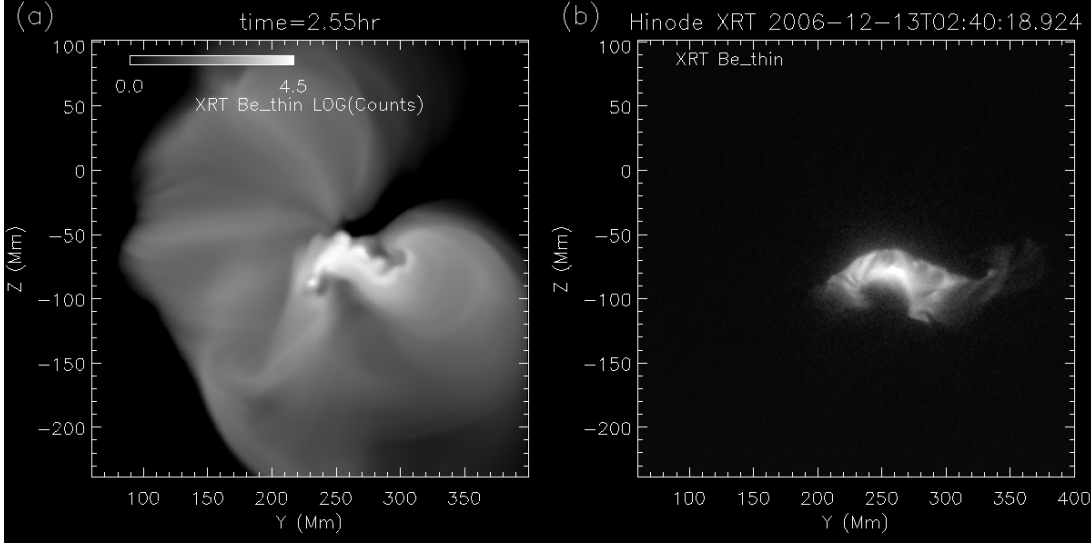


Figure 13. (a) Synthetic Hinode/XRT image at the time of approximately the peak of the magnetic energy dissipation compared to (b) the observed Hinode/XRT image at the time of peaking soft X-ray emission (Schrijver et al. 2008).

the soft X-ray brightening produced by the flare loops is so much higher than that from the surrounding non-flare loops that a much shorter exposure time was used to avoid saturation such that the ambient loops become invisible. On the other hand, the modeled synthetic X-ray images show much less enhancement in the emission from the post-reconnection loops relative to the ambient coronal loops, and thus both remain visible in the dynamic range of the brightness displayed. Here the comparison between the modeled images and the observed ones are merely regarding the qualitative morphological features and is not quantitative. The comparison (see Figure 13) shows that the observed sigmoid shaped band of post-flare loops appears more extended in the east-west direction and shows a less curved hook at its west end. In our simulation, we imposed the emergence of an idealized magnetic torus which only roughly mimics the observed flux emergence pattern (see Figures 1(b) and 1(d)). The resulting emerging bipolar region at the time of the onset of the eruption does not have as large a polarity separation as the observed case, and for the leading (negative) polarity at the west side, the observed flux distribution is more fragmented and extended. These detailed differences can all be contributing to differences in the extension and shape of the current sheet that forms and hence the differences in the extension and shape of the band of the post flare loops that develop.

During the impulsive phase of the eruption, we also see in the movie of the synthetic XRT emission associated with Figure 6, an outgoing band of diffuse brightening that emanates from the sigmoid and moves southward. This outgoing diffuse brightening corresponds to the hot core of the erupting flux rope, whose temperature reaches as high as about 10^7 K, as can be seen in Figures 12(d)(h) which show the erupting flux rope field lines colored with temperature. Such an outgoing brightening feature in soft X-ray produced by an erupting flux rope has been discussed in McKenzie & Canfield (2008). In the Hinode/XRT observation of the present event, the brightening from the post-flare loops dominates and saturates the images (Figure 13(b)) and any disturbances outside of the flaring region are not seen.

Figure 14 shows selected field lines of the erupting flux rope at two time instances during the eruption (top row at $t = 2.55$ hour at about the peak acceleration of the flux rope, and bottom row at $t = 3.69$ hour, when the flux rope begins to exit the domain) and an associated animation which shows the 3D dynamic evolution of the erupting flux rope. The selected field lines are traced from a set of Lagrangian tracers originally placed in the emerged flux rope at the pre-eruption phase (at $t = 2.4$ hour), and tracked in the subsequent velocity field. It can be seen that the initially nearly east-west oriented flux rope has rotated by about 90° counter-clockwise to the nearly south-north oriented final erupting flux rope as shown in Figures 14(d) and 14(e). The initial west (east) leg of the flux rope rotates to become the north (south) leg of the final flux rope exiting the domain. The flank of the north leg of the erupting flux rope with south-ward directed B_z (purple field lines) is adjacent to the sun-earth line, although not yet intersecting the sun-earth line (see Figures 14(d) and 14(e)). The ambient solar wind condition strongly affects the kinematics of the erupting flux rope. Because of the fast wind outflow north of the emerging flux rope as can be seen in Figure 14(c), the northern portion of the erupting flux rope erupts into the fast wind stream, reaching a higher outward speed

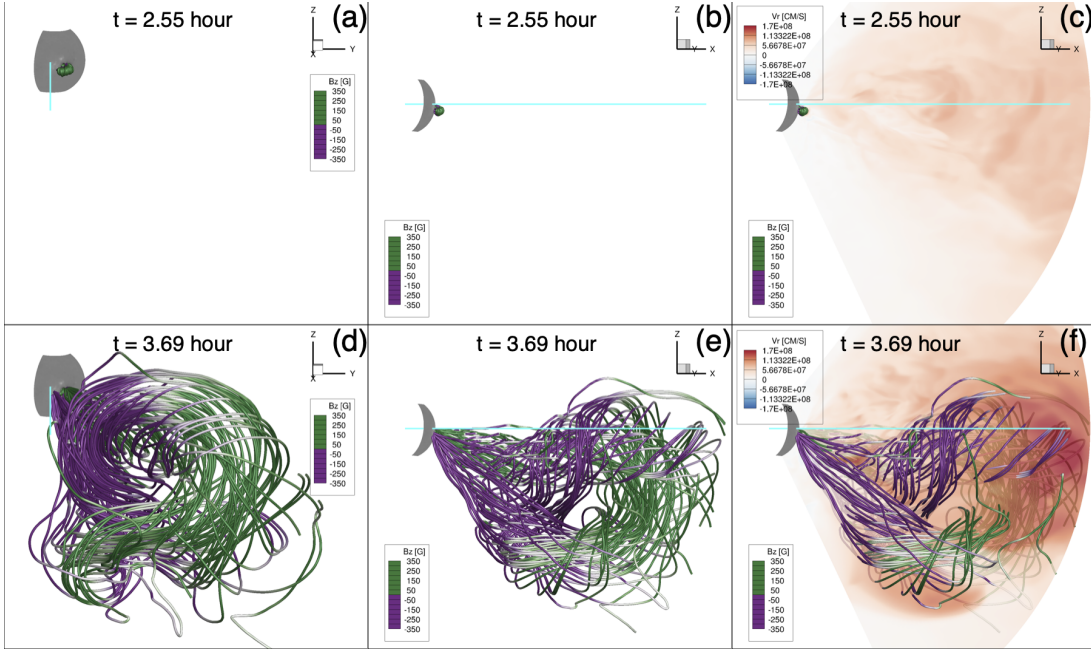


Figure 14. 3D views of selected field lines of the erupting flux rope at $t = 2.55$ hour (top row) and at $t = 3.69$ hour (bottom row), and viewed from an on-disk view point (left column) and from a east-limb view point (middle column). The right column is the same as the middle column but with a middle meridional cross-section across the flux rope added showing the radial velocity. The field lines are colored with the sign of B_z . The cyan line denotes the sun-earth line. An animated version of the images in the left and middle columns are available, which shows the 3D dynamic evolution of the erupting flux rope from $t = 2.4$ hour (just before the onset of the eruption) to $t = 3.69$ hour (when the flux rope begins to exit the domain).

approaching ~ 1700 km/s (Figure 14(f)) and extends out further in the front (Figures 14(d) and 14(e)). The rotation of the erupting flux rope found here (about 90°) is significantly different from that found in Fan (2016), where a much greater rotation of nearly 180° was found. This is caused by both the differences in the imposed lower boundary flux emergence as well as the presence of an ambient solar wind with a partially open magnetic field in this simulation instead of a static, potential field background condition assumed in Fan (2016).

4. SUMMARY AND DISCUSSION

In this work, we have carried out a new simulation of the 13-December-2016 CME event from AR 10930, improving upon the previous simulation by Fan (2016). The improvements include the following. Instead of using a potential magnetic field with a static polytropic atmosphere as the initial state, we have initialized a partially open coronal magnetic field with a background solar wind as the initial state as described in section 2. For the normal magnetic flux distribution at the lower boundary (the base of the corona) of this initial state, we use the normal magnetic field in the horizontal plane at 14 Mm height of the potential field extrapolated from the observed photosphere magnetogram, instead of heavily smoothing the photosphere magnetogram as was done in Fan (2016). The resulting lower boundary normal flux distribution contains a significantly stronger peak field strength (~ 500 G) compared to that in Fan (2016). Furthermore, the current simulation uses a more explicit treatment of the background coronal heating. We impose at the lower boundary a random electric field representing the effect of turbulent convection that drives field-line braiding, and the consequent (numerical) resistive and viscous heating provides the background coronal heating and accelerates the solar wind. Together with this random electric field, we also impose the emergence of a twisted magnetic torus in the way similar to Fan (2016), but is more compact and of a stronger field strength to build up the non-potential, twisted pre-eruption coronal magnetic field of the active region.

With the inclusion of the random electric field which drives a coronal heating that varies spatially and temporally with the formation of the strong current layers in the given 3D coronal magnetic field, we are able to model the synthetic soft X-ray images that would be observed by the Hinode/XRT. It is found that the simulated pre-eruption active region magnetic field, where a twisted magnetic flux rope is built up by the imposed flux emergence, produces synthetic soft X-ray emission that shows qualitatively similar morphology as that observed by the Hinode/XRT, for

both the ambient coronal loops and the central sigmoid that sharpens just before the onset of the eruption. The sharpening of the central sigmoid is due to the formation of a thin sigmoid shaped current layer in the lower part of the flux rope along the central PIL. It is found that at the onset of the exponential acceleration of the flux rope, a significant portion of the emerged flux rope cross-section has entered above the contour of the critical decay index of -1.5 for the onset of the torus instability (e.g. Kliem & Török 2006). Thus the onset of the eruption is consistent with the onset of the torus instability. At the same time we also find that for the central core field lines of the emerged flux rope, the total twist has reached about 1.5 winds, exceeding the critical total twist of 1.25 winds for the onset of the kink instability (e.g. Hood & Priest 1981). This suggests that both the torus instability and the kink instability contribute to driving an unstable rise of the flux rope, which in turn drive the thinning of the central current layer, and the resulting rapid reconnection further leads to the impulsive acceleration of the flux rope.

We find that during the impulsive phase of the eruption, the central sharp thin sigmoid in the synthetic X-ray image broadens to become a bright sigmoid-shaped band, which corresponds to the row of low-lying high-temperature, high-density post-flare loops that form due to the rapid reconnection in the current sheet. The Hinode/XRT observation shows a similar evolution of transitioning from the thin sigmoid to a broadened sigmoid-shaped band of post-flare loops. The agreement is only qualitative. The thin sigmoid at the onset of the eruption appears more westward (by about 10 Mm) in the synthetic image compared to the observed one. In the impulsive phase, the sigmoid-shaped band of post-flare loop brightening in the synthetic XRT image appears less extended towards both the east and west ends, and shows a more curved hook at the west end. Our simulation imposed the emergence of an idealized magnetic torus which only roughly mimics the observed flux emergence pattern. The above discrepancies in the morphology of the soft X-ray emission suggest that a better observationally constrained lower boundary driving of flux emergence is needed to better reproduce the flux rope and the current sheet that form in the realistic coronal magnetic field of the event.

We find that the erupting flux rope accelerates to a peak speed of about 1700 km/s. The erupting flux rope rotates by about 90° counter-clock wise, from an initially nearly east-west oriented emerged flux rope to a final nearly north-south oriented flux rope exiting the domain. The west leg of the initial flux rope rotates to become the north leg of the erupting flux rope, and the flank of the north leg of the flux rope with south-ward directed B_z is adjacent to the sun-earth line, although not yet intersecting the sun-earth line, when the flux rope is exiting the domain. The rotation of the erupting flux rope found here is significantly smaller than that found in Fan (2016), where a rotation of nearly 180° was obtained. This is caused by both the difference in the lower boundary flux emergence as well as the difference in the ambient magnetic field and solar wind conditions. We find that the ambient solar wind condition significantly affects the kinematics of the erupting flux rope. In this case the north portion of the erupting flux rope erupts into the adjacent fast solar wind stream and hence attains a higher erupting speed and extends out further in the front. Thus a better observationally constrained lower boundary driving condition for the emerging active region and also correctly determining the conditions of the ambient coronal magnetic field and the solar wind are all needed to determine the realistic kinematics and the magnetic structure of the outgoing CME.

ACKNOWLEDGMENTS

The author thanks the anonymous referee for helpful comments. This material is based upon work supported by the National Center for Atmospheric Research, which is a major facility sponsored by the National Science Foundation under Cooperative Agreement No. 1852977. This work is also supported by the NASA LWS grant 80NSSC19K0070 to NCAR. The author would like to acknowledge high-performance computing support from Cheyenne (doi:10.5065/D6RX99HX) provided by NCAR's Computational and Information Systems Laboratory, sponsored by the National Science Foundation. Resources supporting this work were also provided by the NASA High-End Computing (HEC) Program through the NASA Advanced Supercomputing (NAS) Division at Ames Research Center.

REFERENCES

- Amari, T., Canou, A., & Aly, J.-J. 2014, *Nature*, 514, 465, doi: [10.1038/nature13815](https://doi.org/10.1038/nature13815)
- Aulanier, G., Janvier, M., & Schmieder, B. 2012, *A&A*, 543, A110, doi: [10.1051/0004-6361/201219311](https://doi.org/10.1051/0004-6361/201219311)

- Bein, B. M., Berkebile-Stoiser, S., Veronig, A. M., et al. 2011, *ApJ*, 738, 191, doi: [10.1088/0004-637X/738/2/191](https://doi.org/10.1088/0004-637X/738/2/191)
- Chen, P. F. 2011, *Living Reviews in Solar Physics*, 8, 1, doi: [10.12942/lrsp-2011-1](https://doi.org/10.12942/lrsp-2011-1)
- Dahlin, J. T., Antiochos, S. K., Qiu, J., & DeVore, C. R. 2022, *ApJ*, 932, 94, doi: [10.3847/1538-4357/ac6e3d](https://doi.org/10.3847/1538-4357/ac6e3d)
- Dahlin, J. T., DeVore, C. R., & Antiochos, S. K. 2021, *ApJ*, submitted. <https://arxiv.org/abs/2112.00641>
- Fan, Y. 2011, *ApJ*, 740, 68, doi: [10.1088/0004-637X/740/2/68](https://doi.org/10.1088/0004-637X/740/2/68)
- . 2016, *ApJ*, 824, 93, doi: [10.3847/0004-637X/824/2/93](https://doi.org/10.3847/0004-637X/824/2/93)
- . 2017, *ApJ*, 844, 26, doi: [10.3847/1538-4357/aa7a56](https://doi.org/10.3847/1538-4357/aa7a56)
- Forbes, T. G., Linker, J. A., Chen, J., et al. 2006, *SSRv*, 123, 251, doi: [10.1007/s11214-006-9019-8](https://doi.org/10.1007/s11214-006-9019-8)
- Green, L. M., Török, T., Vršnak, B., Manchester, W., & Veronig, A. 2018, *SSRv*, 214, 46, doi: [10.1007/s11214-017-0462-5](https://doi.org/10.1007/s11214-017-0462-5)
- Gudiksen, B. V., & Nordlund, Å. 2005, *ApJ*, 618, 1020, doi: [10.1086/426063](https://doi.org/10.1086/426063)
- Guo, Y., Xia, C., Keppens, R., Ding, M. D., & Chen, P. F. 2019, *ApJL*, 870, L21, doi: [10.3847/2041-8213/aafabf](https://doi.org/10.3847/2041-8213/aafabf)
- Hayashi, K., Feng, X., Xiong, M., & Jiang, C. 2018, *ApJ*, 855, 11, doi: [10.3847/1538-4357/aaacd8](https://doi.org/10.3847/1538-4357/aaacd8)
- Hood, A. W., & Priest, E. R. 1981, *Geophysical and Astrophysical Fluid Dynamics*, 17, 297, doi: [10.1080/03091928108243687](https://doi.org/10.1080/03091928108243687)
- Inoue, S., Hayashi, K., Magara, T., Choe, G. S., & Park, Y. D. 2014, *ApJ*, 788, 182, doi: [10.1088/0004-637X/788/2/182](https://doi.org/10.1088/0004-637X/788/2/182)
- Jiang, C., Feng, X., Wu, S. T., & Hu, Q. 2013, *ApJL*, 771, L30, doi: [10.1088/2041-8205/771/2/L30](https://doi.org/10.1088/2041-8205/771/2/L30)
- Kliem, B., Su, Y. N., van Ballegooijen, A. A., & DeLuca, E. E. 2013, *ApJ*, 779, 129, doi: [10.1088/0004-637X/779/2/129](https://doi.org/10.1088/0004-637X/779/2/129)
- Kliem, B., & Török, T. 2006, *Physical Review Letters*, 96, 255002, doi: [10.1103/PhysRevLett.96.255002](https://doi.org/10.1103/PhysRevLett.96.255002)
- Liu, T., Fan, Y., Su, Y., et al. 2022, *ApJ*, in press
- Mackay, D. H., DeVore, C. R., & Antiochos, S. K. 2014, *ApJ*, 784, 164, doi: [10.1088/0004-637X/784/2/164](https://doi.org/10.1088/0004-637X/784/2/164)
- McKenzie, D. E., & Canfield, R. C. 2008, *A&A*, 481, L65, doi: [10.1051/0004-6361/20079035](https://doi.org/10.1051/0004-6361/20079035)
- Min, S., & Chae, J. 2009, *SoPh*, 258, 203, doi: [10.1007/s11207-009-9425-7](https://doi.org/10.1007/s11207-009-9425-7)
- Rempel, M. 2017, *ApJ*, 834, 10, doi: [10.3847/1538-4357/834/1/10](https://doi.org/10.3847/1538-4357/834/1/10)
- Schrijver, C. J., DeRosa, M. L., Metcalf, T., et al. 2008, *ApJ*, 675, 1637, doi: [10.1086/527413](https://doi.org/10.1086/527413)
- Stone, J. M., & Norman, M. L. 1992, *ApJS*, 80, 791, doi: [10.1086/191681](https://doi.org/10.1086/191681)
- Török, T., Downs, C., Linker, J. A., et al. 2018, *ApJ*, 856, 75, doi: [10.3847/1538-4357/aab36d](https://doi.org/10.3847/1538-4357/aab36d)
- Warnecke, J., & Peter, H. 2019, *A&A*, 624, L12, doi: [10.1051/0004-6361/201935385](https://doi.org/10.1051/0004-6361/201935385)
- Withbroe, G. L. 1988, *ApJ*, 325, 442, doi: [10.1086/166015](https://doi.org/10.1086/166015)